


RESEARCH ARTICLE**ROS-mediated anticancer effects of EGFR-targeted nanoceria**

Kochurani K. Johnson^{1,2}  | Pramod Koshy¹ | Chantal Kopecky³ |
 Michelle Devadason⁴ | Joanna Biazik⁵ | Xiaoran Zheng¹ | Yue Jiang¹ |
 Xiaochun Wang⁶ | Yiling Liu³ | Jeff Holst⁴ | Jia-Lin Yang⁶ |
 Kristopher A. Kilian^{1,3} | Charles C. Sorrell¹

¹School of Materials Science and Engineering, Faculty of Science, UNSW Sydney, Sydney, New South Wales, Australia

²Blood Cells and Blood Cancer Division, The Walter and Eliza Hall Institute of Medical Research, Melbourne, Victoria, Australia

³Australian Centre for NanoMedicine, School of Chemistry, Faculty of Science, UNSW Sydney, Sydney, New South Wales, Australia

⁴Translational Cancer Metabolism Laboratory, School of Medical Sciences and Prince of Wales Clinical School, Faculty of Medicine and Health, UNSW Sydney, Sydney, New South Wales, Australia

⁵Electron Microscope Unit, Mark Wainwright Analytical Centre, UNSW Sydney, Sydney, New South Wales, Australia

⁶Prince of Wales Clinical School, Faculty of Medicine and Health, UNSW Sydney, Sydney, New South Wales, Australia

Correspondence

Kochurani K. Johnson, School of Materials Science and Engineering, Faculty of Science, UNSW Sydney, Sydney, NSW 2052, Australia. Email: johnson.k@wehi.edu.au

Funding information

Australian Research Council, Grant/Award Number: DP170104130

Abstract

The therapeutic effectiveness of anticancer drugs, including nanomedicines, can be enhanced with active receptor-targeting strategies. Epidermal growth factor receptor (EGFR) is an important cancer biomarker, constitutively expressed in sarcoma patients of different histological types. The present work reports materials and in vitro biomedical analyses of silanized (passive delivery) and/or EGF-functionalized (active delivery) ceria nanorods exhibiting highly defective catalytically active surfaces. The EGFR-targeting efficiency of nanoceria was confirmed by receptor-binding studies. Increased cytotoxicity and reactive oxygen species (ROS) production were observed for EGF-functionalized nanoceria owing to enhanced cellular uptake by HT-1080 fibrosarcoma cells. The uptake was confirmed by TEM and confocal microscopy. Silanized nanoceria demonstrated negligible/minimal cytotoxicity toward healthy MRC-5 cells at 24 and 48 h, whereas this was significant at 72 h owing to a nanoceria accumulation effect. In contrast, considerable cytotoxicity toward the cancer cells was exhibited at all three time points. The ROS generation and associated cytotoxicity were moderated by the equilibrium between catalysis by ceria, generation of cell debris, and blockage of active sites. EGFR-targeting is shown to enhance the uptake levels of nanoceria by cancer cells, subsequently enhancing the overall anticancer activity and therapeutic performance of ceria.

KEYWORDS

cancer, EGFR, nanoceria, ROS, targeted therapy

1 | INTRODUCTION

Nanomedicines are gaining considerable attention for disease management, particularly cancers. Nanoparticles have been investigated as candidates for drug delivery owing to their small sizes and high surface area to volume ratios, which facilitate adsorption and functionalization.¹ Further, some nanoparticles have intrinsic therapeutic properties,

which allow them to act as anticancer agents and for treatment of other diseases.^{2–4} Cerium oxide nanoparticles or nanoceria (CeO_{2-x}), an oxide of the most abundant rare-earth element cerium,⁵ possesses remarkable intrinsic anticancer properties owing to its pH-dependant redox activity that allows it to switch between Ce³⁺ and Ce⁴⁺ oxidation states,^{6,7} thereby mimicking the activities of superoxide dismutase (SOD) and catalase (CAT) enzymes.^{8,9} These characteristics enable it to act as a

This is an open access article under the terms of the [Creative Commons Attribution-NonCommercial](https://creativecommons.org/licenses/by-nc/4.0/) License, which permits use, distribution and reproduction in any medium, provided the original work is properly cited and is not used for commercial purposes.

© 2023 The Authors. *Journal of Biomedical Materials Research Part A* published by Wiley Periodicals LLC.

prooxidant, inducing the production of reactive oxygen species (ROS) at acidic pH conditions (~ 6.4) of the tumor microenvironment (TME) and as an antioxidant, suppressing the ROS production at basic physiological pH conditions (~ 7.4).^{10,11} Thus, ceria generates ROS-mediated toxic effects on cancer cells^{12,13} while potentially protecting healthy cells and circumventing the unintended side effects of conventional cancer treatments.

Nanoceria commonly occurs in three morphologies: cubes, octahedra, and rods.⁵ Shape is a key factor that can have a profound influence on the biodistribution and pharmacokinetics of the nanoparticles,^{14–16} where the cellular uptake levels of these three morphologies by fibrosarcoma cells has been observed to be in the order rods > cubes > octahedra.⁷ Further, higher peroxidase activity has been reported for nanoceria rods relative to cubes, owing to the former's greater concentrations of Ce^{3+} and charge-compensating O^{2-} vacancies.¹⁷ Size is another critical factor that determines the pharmacokinetic properties and the overall therapeutic performance of nanomedicines.^{18–20} Of the various nanoparticle size ranges that have been fabricated, smaller sizes exhibit greater cellular uptake, where maximal cellular uptake has been reported to be for nanoparticle dimension in the 10–60 nm range.^{19–23} These observations suggest that nanorods of length ≤ 60 nm may enhance bioavailability through increased cellular uptake.

Although ceria can act as an excellent anticancer agent, it is important to ensure its bioavailability at the tumor site in order to achieve the desired therapeutic effectiveness. One of the key issues that have hindered the successful translation of nanomedicines from laboratory scale to clinical scale is the insufficient accumulation of drugs at the tumor site.^{24,25} There are two major mechanisms for the required delivery of drugs to the tumor site. With passive delivery of unfunctionalized nanoparticles, the nanoparticles rely solely on the enhanced permeation and retention (EPR) effect to enter the tumor cells.²⁶ With active delivery of nanoparticles, they are functionalized with biological ligands that recognize and bind to specific receptors on the surfaces of tumor cells.¹⁸ This latter approach can yield significant improvements in the bioavailability of drugs at the tumor site.^{18,27} Biological ligands that have been used for functionalization include peptides, proteins, aptamers, antibodies, and small molecules.²⁸ Further, the targeted delivery of nanomedicines also aids in avoiding the unintentional interaction of drugs with healthy cells, thus minimizing possible side effects.²⁹

Cancer cells overexpress a wide range of receptors, referred to as biomarkers,³⁰ which can serve as excellent candidates for targeted cancer therapies.^{31,32} Of the various biomarkers confirmed in several cancers, epidermal growth factor receptor (EGFR) has been reported as a promising target in many malignancies.^{33,34} The estimated expression levels of EGFR in normal cells is 40,000–100,000 receptors per cell,^{35,36} while an overexpression of more than 10^6 receptors per cell was detected in the malignant cells.^{37,36} EGFR is a promising target especially in sarcoma,^{38–40} where patients exhibit significant molecular tumor heterogeneities, making it difficult to select a potential therapeutic target. While there are many publications on EGFR targeting as a strategy for the treatment of numerous

cancers,^{33,41–44} there are only a few publications reporting it as a targeting agent in sarcoma treatment.^{45–47} In a recent study by Yang et al.,⁴⁸ immunohistochemical analysis revealed an expression of EGFR/HER1 in 78% of a patient population of 46 with soft tissue sarcoma of different histological types. This promising work shows the potential for targeting of EGFR in the treatment of soft tissue sarcomas.

Although previous work has reported the use of EGF for the targeted therapy of cancer,^{49–51} the present work appears to be the first to report the fabrication of EGF-functionalized nanoceria with the aim of enhancing the cellular uptake of nanoparticles and improving the anticancer properties of ceria. Moreover, while the previous studies report the fabrication and application of ceria nanorods in cancer,^{7,52} the current study employs an active delivery strategy with the aim of receptor-targeted delivery of nanorods, thereby making this work the first report of the fabrication of EGF-functionalized ceria nanorods. This approach has widespread applicability as several cancers are EGFR-positive.^{33,53} Further, whereas previous work^{7,52} reports ROS-mediated anticancer effects of nanoceria alone, the present work extends this approach by examining receptor-targeted nanoceria in EGFR-positive cancer. Although the model is human fibrosarcoma, the present work has applications beyond fibrosarcoma because most cancers are EGFR-positive.^{33,53}

Consequently, the present work reports for the first time an investigation into the fabrication of EGFR-targeted ceria nanorods aimed at enhancing the receptor-mediated uptake of nanoceria and subsequent ROS-mediated destruction of fibrosarcoma cells with the aim of facilitating possibilities for EGFR-targeted diagnosis and therapy of EGFR-positive cancers using nanoceria-based formulations. To these ends, nanoceria was fabricated, characterized, and functionalized with EGF protein. The ROS-mediated anticancer effects of EGF-functionalized nanoceria were contrasted with the non-functionalized nanoceria using cell viability testing, ROS measurement assays, cellular uptake studies using inductively coupled plasma mass spectrometry (ICP-MS) and TEM imaging, and western blotting studies. The uptake of EGF-nanoceria also was confirmed using confocal microscopy.

2 | MATERIALS AND METHODS

2.1 | Materials

Cerium nitrate hexahydrate ($\text{Ce}(\text{NO}_3)_3 \cdot 6\text{H}_2\text{O}$), 3-amino-propyl-triethoxysilane (APTES), ethanol ($\text{C}_2\text{H}_5\text{OH}$), methanol (CH_3OH), human epidermal growth factor (hEGF), fluorescein-5-isothiocyanate (FITC), cell counting kit 8 (CCK-8), 2',7'-dichlorodihydrofluorescein diacetate (DCFH-DA), sodium dihydrogen phosphate (NaH_2PO_4), disodium hydrogen phosphate (Na_2HPO_4), RIPA buffer, immobilon-P PVDF membrane, bovine serum albumin (BSA), donkey antirabbit IgG antibody, glutaraldehyde ($\text{C}_5\text{H}_8\text{O}_2$, Electron Microscopy Sciences, USA), procure 812 resin (Electron Microscopy Sciences, USA), lead citrate (ProSciTech, Australia), uranyl acetate (Electron Microscopy Sciences, USA), osmium tetroxide (OsO_4 , Electron Microscopy Sciences, USA), triethanolamine (TEOA,

reagent grade, 99 wt%), 1.0 mM P-benzoquinone (BQ, reagent grade, 98 wt%) and 75 mM isopropyl alcohol (IPA, reagent grade, 99.7 wt%) were purchased from Sigma-Aldrich, Australia. AntiEGFR phospho Y1068 antibody was purchased from Abcam, Australia and PD-MidiTrap G-25 was purchased from Cytiva, Australia. Sodium hydroxide (NaOH), ammonium chloride (NH₄Cl), sodium carbonate (Na₂CO₃), and sodium bicarbonate (NaHCO₃) were purchased from Chem-Supply, Australia. Nitric acid was purchased from RCI Labscan Limited, Australia. Protease inhibitor cocktail was purchased from Roche Diagnostics, Australia and phosphatase inhibitor, EGF Receptor rabbit mAb antibody and β -Actin rabbit mAb antibody were purchased from Cell Signaling Technology, USA. RPMI 1640 medium, DMEM medium, penicillin-streptomycin solution, L-glutamine, Trypsin-EDTA, Dulbecco's phosphate buffered saline (DPBS), Hank's balanced salt solution (HBSS), fetal bovine serum (FBS), Hoechst 33342 solution, 16% w/v paraformaldehyde (PFA; methanol-free), micro BCA protein assay kit, NuPAGE 4%–12% bis-tris gels, and SuperSignal West Pico PLUS Chemiluminescent Substrate were purchased from Thermo Fischer Scientific, Australia. HT-1080 and MRC-5 cell lines were purchased from American Type Cell Culture (ATCC), USA.

2.2 | Synthesis of nanoceria

Rod-shaped cerium oxide nanoparticles were synthesized using a previously described hydrothermal technique.⁵ In the synthesis process, 8.6844 g of Ce (NO₃)₃·6H₂O and 24 g of NaOH were added to a 100 mL Pyrex beaker to achieve concentrations of 0.5 M and 15 M, respectively, in 40 mL deionized (DI) water. The solution was stirred for 30 min at room temperature using a magnetic stirrer. The solution was transferred to a 50 mL Teflon-lined autoclave reactor for hydrothermal reaction at 60°C for 48 h (heating rate 5°C/min). After synthesis, the nanoparticles were separated from the medium by centrifugation at 5000 rpm (2935 × g) for 20 min and decanting. The nanoparticles then were cleaned by the following steps applied repeatedly 16–18 times by alternate resuspension in 25 mL of DI water and 25 mL ethanol, sonication for 10 min, centrifugation at 5000 rpm (2935 × g) for 20 min, and decanting. This extent of washing was required for complete removal of Na. The nanoparticles finally were transferred to an opaque glass container, air-dried at 60°C for 12 h in an oven, and readied for long-term storage by sealing with a screw-cap lid.

2.3 | Functionalization of nanoceria

Nanoceria was coated using APTES as a linker for the conjugation of EGF/EGF-FITC. Silanization was performed by dropwise addition of 1.5 mL APTES to 100 mg of nanoceria suspended in 25 mL of ethanol, sonication for 10 min, and magnetic stirring for 24 h, as described elsewhere.⁵⁴ The APTES-coated nanoparticles were cleaned by the following steps applied repeatedly 5 times by resuspension in 25 mL ethanol, sonication for 10 min, centrifugation at 5000 rpm (2935 × g) for 20 min, and decanting. The nanoparticles finally were transferred

to a clear glass container, air-dried at 60°C for 12 h in an oven, and readied for short-term storage by sealing with a screw-cap lid.

The conjugation of EGF onto the APTES-modified nanoparticles was done according to the variant of a protocol described elsewhere.⁵⁵ This which involves the mixing of APTES-coated nanoparticles with the peptide in the presence of 10 vol% ethanol. This allows the binding of the carboxyl groups of the peptide with the amine groups of APTES through covalent attachment.⁵⁵ 100 mg of APTES-coated nanoceria were suspended in 10 vol% ethanol in DPBS, which were conjugated by the addition of 50 μ g of EGF in order to achieve an EGF working concentration of 16 nM. The suspension was mixed using a rotary tube mixer (WiseMix RT-10, Korea) at 20 rpm at 4°C for 14–16 h. After functionalization, the EGF-functionalized nanoparticles were separated from the medium by ultracentrifugation (Optima XPN Beckman-Coulter, USA, SW 41 Ti swinging-bucket rotor) at 30,000 rpm (154,000 × g) for 10 min at 4°C and decanting. Subsequent purification involved the following steps applied twice by resuspension in variable amounts of 10 vol% ethanol in DPBS according to the nanoparticle amount, ultracentrifugation at 30,000 rpm for 10 min at 4°C, and decanting. The particles obtained after purification were resuspended in Milli-Q water, lyophilized (Christ Alpha 1–4 LDplus, Germany; –54°C, 1–4 × 10^{–6} kPa) and stored at –20°C for further use. Since the potential desorption of proteins from nanoparticles happen in the liquid state, it is assumed that the desorption does not occur during the period in which the materials are frozen.

FITC-labeled EGF was obtained according to a variant of a process described elsewhere⁵⁶ and then conjugated to APTES-nanoceria for confocal imaging studies. EGF was labeled with FITC by mixing FITC and EGF in 1:10 weight ratio in a solution of 0.1 M carbonate buffer at pH 9.0 using a rotary tube mixer at 20 rpm at 4°C under dark conditions for 14–16 h. This was followed by the addition of 1 M NH₄Cl in order to inactivate the residual FITC. The FITC-labeled protein was purified using a Sephadex G-25 column and stored at –20°C for long-term use. For subsequent conjugation to the APTES-nanoceria, the immediately preceding process was used.

2.4 | Characterization of nanoparticles

The morphological characteristics (size and shape) of nanoparticles were analyzed using transmission electron microscopy (TEM; FEI Tecnai G2 20 TEM, USA; 200 kV). The nanoparticles (~0.5 mg) were dispersed in 0.5 mL of methanol, sonicated for 3 min, loaded on copper grids, and dried at 37°C for 24 h before imaging. The mineralogy of nanoceria was determined by x-ray diffraction (XRD; Philips X'Pert Multipurpose x-ray Diffractometer (MPD), Netherlands; CuK α , step size 0.02° 2 θ , scanning speed 5.5° 2 θ min^{–1}) and laser Raman microspectroscopy (Renishaw inVia Raman microscope, UK; 35 mW, helium-neon green laser, 514 nm). The chemical bonding natures of the nanoceria, APTES-nanoceria, and EGF-nanoceria were assessed using Fourier transform infrared spectroscopy (FTIR) with attenuated total reflectance (ATR) (PerkinElmer Spectrum Two FT-IR spectrometer, USA; resolution 4 cm^{–1}) and thermogravimetric analysis (TGA; NETZSCH STA 449F1, Germany;

temperature range 25 to 500°C in air, 200 mL/min flow rate, aluminum crucible). The surface chemistry of the nanoceria, APTES-nanoceria, and EGF-nanoceria was examined using x-ray photoelectron spectroscopy (XPS; Thermo Fisher Scientific, ESCALAB 250Xi spectrometer, UK; AlK α , 13.8 kV, 8.7 mA, spot size 500 μ m). For the suspensions of APTES-nanoceria and EGF-nanoceria, the hydrodynamic size distributions and the zeta potentials were measured using dynamic light scattering (DLS; Malvern Zetasizer Nano ZS, UK; 10 mW, 633 nm He-Ne laser). Although the suspensions were sonicated for 3 min prior to measurement, the nanoparticles were agglomerated. The photocatalytic nature of nanoceria was analyzed using the methylene blue (MB) degradation assay.⁵⁷ 8 mg of nanoparticles were added to 8 mL of MB dye solution in a 50 mL Pyrex beaker, followed by adding 10.0 mM concentrations of triethanolamine, 1.0 mM P-benzoquinone, and 75 mM isopropyl alcohol. The testing was done using magnetic stirring at 300 rpm for 15 min while in the dark in a light-obstructed black box. The sample was exposed to 365 nm UV irradiation from a UV lamp (8 W, 3UV-38, UVP) while being magnetically stirred at 300 rpm for different times up to 1 h in the black box. The UV-Vis testing was done on the solution following nanoparticle removal by centrifugation.

2.5 | Cell culture

Human fibrosarcoma cells (HT1080) were cultured in RPMI medium, supplemented with 10 vol% FBS, 1 vol% penicillin-streptomycin, and 2.0 mM L-glutamine, and incubated at 37°C under 5 vol% CO₂ atmosphere. The human fibroblast cell line (MRC-5) was cultured in DMEM medium, supplemented with 10 vol% FBS, 1 vol% penicillin-streptomycin, and 2.0 mM L-glutamine, and maintained at 37°C under 5 vol% CO₂ atmosphere.

2.6 | Dose-dependent cytotoxicity of nanoceria

The dose-dependent cytotoxicity of nanoceria on fibrosarcoma cells was assessed by a cytotoxicity assay using the CCK-8. CCK-8 assay is a standard test⁵⁸⁻⁶¹ used to measure cell viability based on the activity of the dehydrogenase enzyme present in the cells, which reduces the pink CCK-8 reagent WST-8 [2-(2-methoxy-4-nitrophenyl)-3-(4-nitrophenyl)-5-(2,4-disulphophenyl)-2H-tetrazolium, monosodium salt] to the orange formazan reaction product.⁶² HT1080 cells were seeded in a 96-well plate at a seeding density of 1000 cells/well with 100 μ L RPMI per well and incubated for 24 h. The medium in each well was replaced with different concentrations of APTES-nanoceria suspensions prepared in RPMI medium, ranging from 100 to 500 μ g/mL (100, 200, 300, 400, and 500 μ g/mL). The nanoparticle suspensions were ultrasonicated for 3 min prior to addition to the cells so as to disperse the nanoparticle agglomerates. The success of this de-agglomeration process was shown by the absence of sedimentation over the following 3–5 min. The medium in the control wells were replaced simultaneously with fresh RPMI medium. Six wells were used for each concentration. The plates then were incubated for

48 h. After incubation, 10 μ L of CCK-8 reagent were added to each well and incubated for 3 h. RPMI (100 μ L) mixed with CCK-8 reagent (10 μ L) were used as the blank. The optical absorbance at 450 nm was determined using a microplate reader (CLARIOstar plus, BMG LABTECH, Germany). Nanoceria control wells were employed in the present work in order to determine the absorbance of nanoparticles alone at 450 nm; any absorbance from the nanoparticles was deducted from the absorbance values obtained for the test wells before calculating the percent cell viability.

2.7 | Cell viability assay

HT1080 cells were seeded in three 96-well plates at a seeding density of 1000 cells/well and incubated for 24 h. The medium was removed and replaced with 100 μ L of fresh RPMI in the control wells and with 100 μ L of functionalized/nonfunctionalized nanoceria in the test wells at 200 μ g/mL concentration. The nanoparticle suspensions were ultrasonicated for 3 min prior to addition to the cells so as to disperse the nanoparticle agglomerates. The success of this de-agglomeration process was shown by the absence of sedimentation over the following 3–5 min. Six wells per test sample were used. The plates then were incubated for 24, 48, or 72 h. After the respective incubation periods, CCK-8 reagent (10 μ L) was added to each well, incubated for 3 h, and the optical absorbance at 450 nm was measured.

2.8 | Testing the effect of cell debris on the active sites of nanoceria

In order to generate cell debris, HT1080 cells were seeded in a 96-well plate at a seeding density of 4000 cells/well and incubated for 24 h. The medium was removed and replaced with 100 μ L of 1X DPBS and the plate was incubated for a further 4 h in order to kill the cells. The cell debris were collected and diluted with RPMI. In order to perform the cell viability assay, HT1080 cells were seeded in three 96-well plates at a seeding density of 4000 cells/well and incubated for 24 h. The medium was removed and replaced with 100 μ L of fresh RPMI in the control wells and with 100 μ L of nanoceria (non-functionalized) in six test wells at 200 μ g/mL concentration. 50 μ L of 400 μ g/mL nanoceria and 50 μ L of cell debris suspension was added to the remaining six test wells in order to make a final concentration of 200 μ g/mL. The nanoparticle suspensions were ultrasonicated for 3 min prior to addition to the cells so as to disperse the nanoparticle agglomerates. Six wells per test sample were used. The plates then were incubated for 48 h. After the incubation time, CCK-8 reagent (10 μ L) was added to each well, incubated for 3 h, and the optical absorbance at 450 nm was measured.

2.9 | Measurement of cellular ROS

Cellular ROS generation levels in cancer cells were measured using the DCFDA assay as described elsewhere^{7,52} with a few

modifications. HT1080 cells were seeded as described immediately above and treated with 200 µg/mL of functionalized or nonfunctionalized nanoceria and incubated for 24, 48, or 72 h. The nanoparticle suspensions were ultrasonicated for 3 min prior to addition to the cells so as to disperse the nanoparticle agglomerates. The success of this de-agglomeration process was shown by the absence of sedimentation over the following 3–5 min. After the respective incubation periods, the cells were washed with 1X DPBS and then 1X trypsin (100 µL) was added to each well. The plate was incubated for 5 min and then 2',7'-dichlorodihydrofluorescein diacetate (DCFH-DA) in HBSS (10 µM) were added in order to achieve a final concentration of 5 µM, followed by incubation for 40 min. The fluorescence intensities at 485 and 535 nm then were determined.

2.10 | Quantification of cellular uptake of nanoceria

ICP-MS is a highly sensitive technique employed in the quantification of cellular uptake of metal or metal oxide nanoparticles⁶³ and thus was used to quantify the cellular uptake of nanoceria. HT1080 cells were seeded in 24-well plates at a seeding density of 4000 cells/well and incubated for 24 h. The RPMI in the wells was replaced with 200 µg/mL of functionalized or nonfunctionalized nanoceria and incubated for 24, 48, or 72 h. The nanoparticle suspensions were ultrasonicated for 3 min prior to addition to the cells so as to disperse the nanoparticle agglomerates. The success of this de-agglomeration process was shown by the absence of sedimentation over the following 3–5 min. Six wells per test sample were used. After the respective incubation periods, the nanoceria suspension was discarded and the cells were washed thrice with 1X DPBS. Trypsin (500 µL) was added and the plates incubated for 5 min. Trypsinized cells then were digested completely using concentrated nitric acid. The cerium content in each sample was quantified using inductively coupled plasma mass spectrometry (ICP-MS; PerkinElmer quadrupole NexION, USA). Untreated cells were used as controls for quantification.

2.11 | Western blotting tests

HT1080 cells were seeded at a seeding density of 0.5×10^6 cells per well in 6-well plates. Three such plates were seeded in order to study the receptor stimulation after 5, 30, or 60 min. The RPMI in the wells was replaced with serum-free RPMI and the plates were incubated for 14–16 h. The cells then were treated with serum-free RPMI with or without 200 µg/mL EGF-nanoceria and incubated for 5, 30, or 60 min. The nanoparticle suspension was ultrasonicated for 3 min prior to addition to the cells so as to disperse the nanoparticle agglomerates. The success of this de-agglomeration process was shown by the absence of sedimentation over the following 3–5 min. The medium was removed and the cells were washed thrice with cold DPBS before being lysed at 4°C with lysis buffer containing protease inhibitor cocktail and phosphatase inhibitor. The protein concentration was quantified for each sample using the Micro BCA protein

assay kit. Equal amounts of protein were loaded onto 4–12 wt% bis-tris gels and transferred to PVDF membranes following electrophoresis. The membranes were blocked with gentle agitation for 1 h using 5% (w/v) BSA in TBST (tris-buffered saline with tween-20) and incubated for 14–16 h with primary antibodies against phosphorylated EGFR (phospho Y1068), EGFR and β-actin. The membranes Then were washed with TBST for three 5-min intervals and incubated (1 h at 25°C with gentle agitation) with donkey antirabbit IgG antibody conjugated with horseradish peroxidase (HRP). The membranes were washed with TBST for three 5-min intervals and visualized with enhanced chemiluminescence reagents (ECL) using an ImageQuant LAS 4000 Biomolecular Imager (GE Healthcare, UK).

2.12 | Imaging of cellular uptake of nanoceria using transmission electron microscopy

HT1080 cells were seeded in 24-well plates at a seeding density of 10,000 cells/well, with sterilized cover slips placed inside each well. Following incubation for 24 h, the RPMI medium in the wells was discarded and the cells were treated with functionalized or nonfunctionalized nanoceria at a concentration of 200 µg/mL and incubated for 1, 2, 5, or 30 min. The nanoparticle suspensions were ultrasonicated for 3 min prior to addition to the cells so as to disperse the nanoparticle agglomerates. The success of this de-agglomeration process was shown by the absence of sedimentation over the following 3–5 min. The nanoparticle suspension was discarded from each well and the cells were washed thrice with 1X DPBS. The cells were fixed overnight at 4°C in a fixative comprised of 2.5% (w/v) glutaraldehyde in 0.2 M sodium phosphate buffer (pH 7.4). Fixed cells were rinsed with 0.1 M sodium phosphate buffer and post-fixed in 1% (w/v) osmium tetroxide in 0.2 M sodium phosphate buffer using a BioWave Pro+ Microwave Tissue Processor (Ted Pella, USA). After rinsing with 0.1 M sodium phosphate buffer, the samples were dehydrated in a graded ethanol series (50, 70, 80, and 90 vol% ethanol OH for 10 min each followed by 100 vol% ethanol twice for 10 min each). They then were infiltrated with resin (Procore 812, Electron Microscopy Sciences, USA) and polymerized in an oven at 60°C for 48 h. Ultrathin sections (70 nm) were cut using a diamond knife (Diatome, Switzerland) and collected onto carbon-coated copper-slot TEM grids. The grids were post-stained using uranyl acetate (2% w/v) and lead citrate. Two grids for each sample were imaged by TEM (JEOL 1400, Japan; 100 kV).

2.13 | Imaging of cellular uptake of nanoceria using confocal microscopy

For confocal imaging studies, HT1080 cells were seeded in 12-well glass-bottom plates at a seeding density of 40,000 cells/well and incubated for 24 h. Triplicate wells were used for each test. After 24 h of incubation, the RPMI in the wells was replaced with 200 µg/mL FITC-tagged EGF-conjugated nanoceria and the plates were incubated for 5 min, 30 min, or 5 h. The nanoparticle suspension was ultrasonicated for 3 min prior to addition to the cells so as to disperse the nanoparticle agglomerates.

The success of this de-agglomeration process was shown by the absence of sedimentation over the following 3–5 min. After incubation, the cells were washed three times with 500 μL of 1X DPBS and stained with 500 μL of Hoechst 33342 DNA stain which was diluted in the ratio 1:1000 using RPMI. The cells were washed with 500 μL of DPBS and fixed with 500 μL of 4% (w/v) PFA solution. After fixation, the cells were washed thrice with 500 μL of DPBS. The cells were imaged using confocal laser scanning microscopy (Zeiss LSM 800, Germany) using a Plan-Apochromat 20X/0.8 M27 and excitation/emission wavelengths were at 488/400–700 nm/1.13 AU for FITC and 405/400–510 nm/1.21 AU for Hoechst with a Notch filter applied for both channels at the respective excitation wavelengths. High resolution images were obtained using a Plan-Apochromat 63X/1.40 Oil DIC M27 and excitation/emission wavelengths were at 488/400–700 nm/0.82 AU for FITC and 405/400–510 nm/0.88 AU for Hoechst with a Notch filter applied for both channels at the respective excitation wavelengths.

2.14 | Biocompatibility of nanoceria (cell viability assay – cancer cells vs. normal cells)

HT1080 cells and MRC-5 cells were seeded in 96-well plates and treated with APTES-nanoceria suspension as described in the cell viability assay protocol. RPMI medium (HT1080 cells) and DMEM medium (MRC-5 cells) were used for the seeding and the preparation of the nanoparticle suspensions. The nanoparticle suspensions in the wells were discarded after incubation for 24 h and replaced with fresh medium every 24 h. Untreated cells were used as controls. After incubation for 24, 48, or 72 h, CCK-8 reagent was added and the optical absorbance at 450 nm was measured.

2.15 | Statistical analysis

All statistical analyses were performed using GraphPad Prism software and the data are represented in terms of the mean and the standard error of the mean (SEM; error bars). One-way analysis of variance (ANOVA) or two-way analysis of variance was used for the analysis; P values that were less than 0.05 were considered statistically significant: * $p \leq .05$, ** $p \leq .01$, *** $p \leq .001$, and **** $p \leq .0001$.

3 | RESULTS AND DISCUSSION

3.1 | Fabrication, modification, and characterization of nanoparticles

TEM direct imaging of hydrothermally synthesized nanoceria revealed a rod-shaped morphology and extensive agglomeration. The differential shadowing of overlapping nanorods as shown in Figure S1 (Data S1) indicates the general absence of intergrowths, so the nanorods are monodisperse and soft agglomerates formed only during mounting using methanol. A summary of the average dimensions of the nanoparticles determined from TEM images is given in Table 1.

The spread of these data is such that no conclusion concerning the probable locations of the conjugated species can be made.

The mineralogical analyses by XRD and laser Raman microspectroscopy in Figure S2 (Data S1) confirm that hydrothermal synthesis yielded single-phase CeO_2 ,^{64–67} which crystallizes in the face-centered cubic fluorite structure.⁶⁸ The Raman data reveal the presence of a detectable concentration of oxygen vacancies [$\text{V}_\text{O}^\bullet$], as shown by the peak at 590 cm^{-1} .

The XPS analyses results and the FTIR spectra data of the nanoparticles are explained in the Data S1 (Figures S3 and S4, and Tables S1 and S2). Coating with APTES and functionalization with EGF was further confirmed using TGA analysis as shown in Figure S5 and explained in the Data S1. The photocatalytic property of nanoceria was also tested using the methylene blue degradation assay as shown in Figure S6.

The DLS analyses shown in Figure S7 and Table S3 illustrate the hydrodynamic diameters, which were interpolated visually from the curves, and the zeta potentials of the nonfunctionalized (APTES-nanoceria) and functionalized (EGF-nanoceria) materials. Although the ceria morphology is nanorod, Figure 6 indicates that the morphology of the agglomerates is spherical.

The average hydrodynamic diameters of APTES-nanoceria and EGF-nanoceria were calculated from the digital output to be 134.3 ± 10.1 nm and 165.2 ± 31.7 nm, respectively. The opposite surface charges of these as well as the increase in average hydrodynamic diameter is attributed to the functionalization by the negatively charged EGF protein⁶⁹ onto the surfaces of the APTES-nanoceria. The tendency to agglomerate is consistent with these zeta potentials, which are less than the well-known threshold of <30 mV for agglomeration.⁷⁰

3.2 | Dose-dependent cytotoxicity of nanoceria on fibrosarcoma cells

In order to evaluate the impact of nanoceria dosage on the viability of tumor cells and to determine the optimal nanoceria concentration that can be employed for targeting, HT-1080 cells were exposed to APTES-coated nanoceria (nonfunctionalized nanoceria) of different concentrations varying in the range 100–500 $\mu\text{g}/\text{mL}$ for 48 h. Figure 1 shows that the viability of HT-1080 cells decreased logarithmically with increasing nanoceria concentration, where the minimal dose that can induce ~50% cell death (IC50 value) was in the range 200–300 $\mu\text{g}/\text{mL}$. Since visualization of the cells was significantly occluded at the higher concentration of 300 $\mu\text{g}/\text{mL}$ (53.1% cell death), the lower concentration of 200 $\mu\text{g}/\text{mL}$ (43.5% cell death) was used for all further testing.

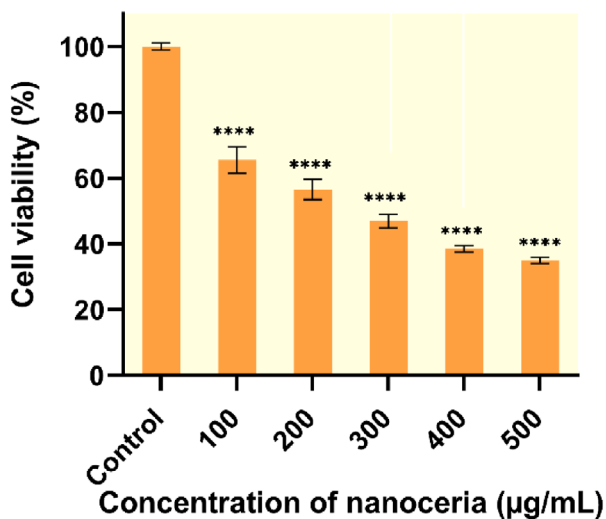
3.3 | Enhanced anticancer activity of EGF-functionalized nanoceria

The influence of EGF functionalization on the ability of nanoceria to kill cancer cells was determined by performing a cell viability assay after treating the HT-1080 cells with nanoceria or EGF-nanoceria for 24, 48, and 72 h. The cell viability results of Figure 2 show that the cytotoxicity of nanoceria toward fibrosarcoma cells at all-time points

TABLE 1 Average dimensions of nanoceria rods (100–120 measurements).

Dimension	Pristine nanoceria	APTES-nanoceria	EGF-nanoceria
Length	83.9 ± 27.3 nm	92.2 ± 23.5 nm	102.1 ± 28.2 nm
Width	12.4 ± 1.6 nm	12.1 ± 0.9 nm	10.2 ± 2.1 nm

Abbreviations: APTES, amino-propyl-triethoxysilane; EGF, epidermal growth factor.

**FIGURE 1** Impact of nanoceria concentration on viability of HT-1080 cells (48 h), **** represents difference from control.

was superior for the EGF-nanoceria treated cells compared to the APTES-nanoceria treated cells. However, the cytotoxicity decreased with increasing time. This is attributed to the blockage of the catalytically active sites,^{71–74} which generally are considered to be oxygen vacancies.^{75,76} This blockage is likely to have been caused by the organic cell debris created during necrosis and apoptosis.^{77,78} This conclusion is supported by the XPS analyses, which show the unavoidable adventitious carbon that adsorbs on the surfaces of solids,⁷⁹ Figure S3 (Data S1) confirms the gradual adsorption of carbonaceous species while Figures S4a and S4b confirm the presence of numerous organic species. The effect of cell debris on the activity of nanoceria was confirmed further by performing a cell viability assay using nanoceria in the presence or absence of cell debris, as shown in Figure S8. The data suggest a decrease in the cytotoxicity of nanoceria with the presence of cell debris, as can be seen by the decreased cell death induced by the nanoceria in the samples where cell debris were present.

Further, the trends for both APTES-nanoceria and EGF-nanoceria are exponential with time but the rate of decrease in cytotoxicity is greater for the former. As these data show both extents of cell death and the generation of debris, the absence of identical trends indicates that the nature of the cell fragmentation upon death is different for each type of nanoceria. That is, APTES-nanoceria appears to generate either more debris or debris that contain ionic species more likely to be adsorbed in the oxygen vacancies. Further, the decrease in cell viability for EGF-nanoceria treated cells in comparison with APTES-nanoceria

treated cells was observed consistently at all the time points studied. However, viability percentage of treated cells shows a decreasing trend with respect to increasing time points. This might be due to the saturation level of ROS generation already attaining around 48 h.

Another potential factor affecting the performance could be the change in pH caused by (1) cell death and release of debris and/or (2) cell division. In the former case, this would be likely to decrease the pH owing to the lower pH in the TME. In the latter case, the pH again would be likely to decrease as the metabolites released during this process are known to be acidic.⁸⁰ Since the production of the ROS that are responsible for cancer cell apoptosis increases in acidic environments,⁸¹ then this should decrease the cell viability with time, which is opposite of the observations.

Finally, a third type of potential factor is the potential recovery of the cancer cells.⁸² However, recovery is enabled by the use of inadequate dosages of drugs and the present work was done using a concentration approximating the IC50 value. As this cannot be considered to be inadequate, then it is unlikely that the data reflect this effect.

Since the cytotoxicity of nanoceria is ROS-mediated,^{83,84} the nanoceria-induced generation of cellular ROS was measured after treating the cells with APTES-nanoceria or EGF-nanoceria. There is only a subtle border between the prooxidant and antioxidant nature of nanoceria and it is strongly pH-dependant.⁸⁵ Seminko et al.⁸⁵ have studied this pH-dependant ROS generation feature of nanoceria and reported the formation of different ROS types in hydrogen peroxide-nanoceria water solutions with different pH values. Since the present work aims at the potential improvement of ROS generation capability of EGF-functionalized nanoceria in cells, an assay that can measure the cellular ROS levels was employed. The DCFDA assay was used in order to measure the ROS production and the level of ROS generation was compared for the nonfunctionalized and functionalized nanoceria treated cells after 24, 48, or 72 h of treatment. Figure 3 reveals the general observation that ROS generation, which is proportional to the fluorescence intensity, was superior for the EGF-nanoceria compared to that of the APTES nanoceria. The additional detailed observations that can be made about these data are as follows:

1. APTES-nanoceria and EGF-nanoceria exhibit greater ROS production capabilities because they contain nanoceria, which generates ROS through catalysis at the active sites.
2. Control cells undergo active proliferation over time, which results in a gradual increase in the generation of ROS over time. The significant increase in the ROS-production levels for the control cells between 48 and 72 h is attributed to the oxidative stress

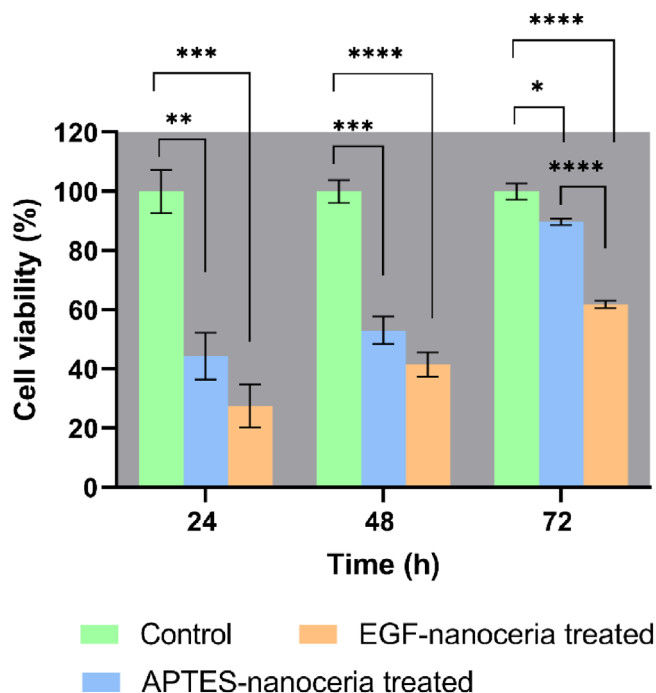


FIGURE 2 Influence of EGF functionalization on viability of HT-1080 cells, * $p \leq .05$, ** $p \leq .01$, *** $p \leq .001$, and **** $p \leq .0001$. EGF, epidermal growth factor.

induced by the accumulation of acidic metabolites in the growth medium, which was not changed, over time.

3. A counter-intuitive observation is the significant decrease in the ROS levels for the APTES-nanoceria treated cells between 48 and 72 h. This phenomenon is attributed to the hydrolysis of the three germinal Si-OEt groups of APTES (Graphical abstract), which generates three terminal silanol (Si-OH) groups, each O ion of which can occupy an oxygen vacancy (i.e., active site).^{86,87}
4. There is a second potential mechanism to explain the decrease in ROS levels. The occupation of an oxygen vacancy by an oxygen ion neutralizes the 2+ charge of the oxygen vacancy (V_O^{2+}). The loss of these two electrons must be charge compensated by the addition of two electrons from the environment. These electrons can be provided by the ROS superoxide ($^{\bullet}O_2^-$), which is not detected by the DCFDA assay that was used.⁸⁸ The neutralization of this ROS will suppress the formation of the ROS H_2O_2 , which is well known as the SOD reaction,⁸⁹ which occurs in the acidic conditions that were used, and is detected by the DCFDA assay that was used.⁸⁸ This process explains the decrease in ROS.
5. However, regardless of the elimination of the active site V_O^{2+} by occupation of O ion of the silanol group and/or neutralization of the ROS by charge compensation by the ROS $^{\bullet}O_2^-$, there occurs a continued production of ROS and cell death induced by nanoceria, as evident from the cell viability results at 72 h, which reveal overall increases in ROS production for both APTES-nanoceria treated cells and EGF-nanoceria treated cells.
6. Despite of the continued generation of ROS, cell death induced by APTES-nanoceria is relatively low at 72 h, as shown in Figure 2.

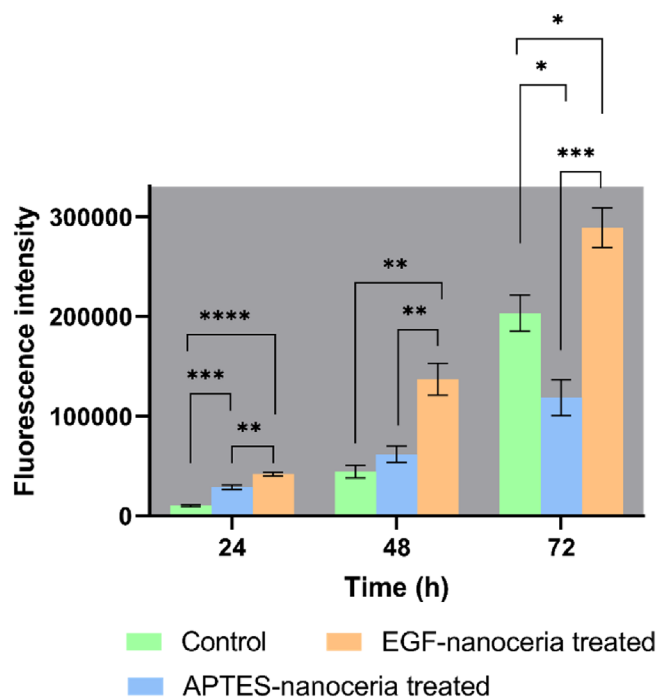


FIGURE 3 Cellular ROS generation levels in APTES-nanoceria treated and EGF-nanoceria treated HT-1080 cells, * $p \leq .05$, ** $p \leq .01$, *** $p \leq .001$, and **** $p \leq .0001$. APTES, amino-propyl-triethoxysilane; EGF, epidermal growth factor; ROS, reactive oxygen species.

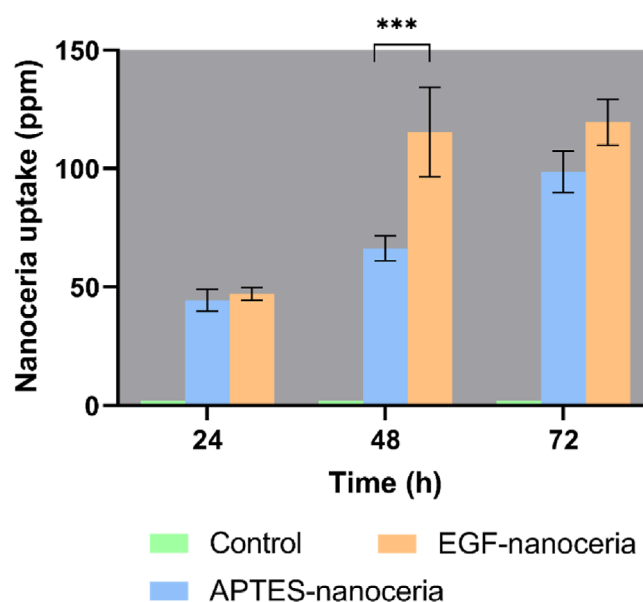


FIGURE 4 Cellular uptake levels of APTES-nanoceria and EGF-nanoceria by HT-1080 cells measured by ICP-MS, *** $p \leq .001$. APTES, amino-propyl-triethoxysilane; EGF, epidermal growth factor; ICP-MS, inductively coupled plasma mass spectrometry.

This is attributed to the comparative rates of ROS production (causing cell death) vs cell debris production (causing blockage of active sites and suppression of cell death by catalysis), where the latter exceeds the former.

7. ROS production for EGF-nanoceria treated cells at 72 h is significantly greater than that for APTES-nanoceria treated cells. This is consistent with the significantly decreased cell viability relative to that of APTES-nanoceria treated cells. This is attributed to (1) reduced blockage of active sites owing to the absence of the Si-O group in EGF, (2) enhanced uptake from the receptor-mediated endocytosis, and (3) further enhancement of the uptake owing to the greater biocompatibility of EGF-functionalized nanoceria.

This discussion indicates that EGF as a biocompatible and stable functionalizing agent represents an advantageous strategy for targeted delivery of nanoparticles and subsequent cancer therapy.

Figure 4 shows the HT-1080 cellular uptake levels of nonfunctionalized and functionalized nanoceria. The results demonstrate no significant enhancement in the uptake of EGF-functionalized nanoceria at 24 h although the two longer time points show significant enhancement. The HT-1080 cells appear to have reached the maximal uptake of EGF-nanoceria after 48 h, as indicated by the equivalence of the data. In contrast, the uptake of APTES-nanoceria is exponential, which indicates the slower uptake owing to passive delivery whereas the EGF-nanoceria uptake is accelerated by active delivery owing to the presence of the receptor-mediated endocytosis.⁹⁰

However, the cellular uptake and ROS production are semi-dependent variables, where the latter depends on the former, but the former is essentially independent of the latter. That is, once uptake occurs, then ROS production commences. As discussed above, following uptake, the processes of overproduction of ROS, cell death, debris generation and adsorption, and blockage of active sites can occur. These would affect the population of cells capable of uptake of nanoceria, thus effectively decreasing the uptake. Thus, this mechanism represents an alternative, which is noncontradictory, to that based on maximal uptake by cells.

3.4 | Interaction of EGF-nanoceria with EGF receptor

Western blot analysis was performed in order to confirm the EGFR binding specificity of EGF-functionalized nanoparticles. After the treatment with nanoceria for 5, 30, or 60 min, the medium containing

the nanoparticles was discarded and the cells were washed thoroughly with DPBS. This washing step ensured the removal of residual nanoparticles and therefore any possible desorbed EGF, thus ensuring the interaction between the EGF conjugated to the nanoparticles and the receptor, thereby providing a measure of the EGF-nanoceria induced phosphorylation of EGFR. Figure 5 confirms the EGF-induced phosphorylation of the receptor, as evidenced by the presence of p-EGFR bands in the samples treated with EGF-nanoceria for 5 and 30 min. The diminishing of the band in the sample treated for 30 min and the absence of p-EGFR band in the cell sample treated for 60 min is attributed to the dephosphorylation of the receptor.⁹¹ The time-dependence of these processes; which include receptor-binding of EGF-nanoceria, phosphorylation, de-phosphorylation, and further downstream signaling; is supported by the observation of the progressively diminishing p-EGFR band intensities with time. The diminishing of p-EGFR band intensities further confirms the absence of any free EGF moieties in the nanoparticle formulation. The intensities of the protein EGFR bands correlate with those of the p-EGFR in the EGF-nanoceria treated cell lysates, thus confirming the stimulation of EGFR by EGF-nanoceria. The EGF-nanoceria interacts rapidly with the HT-1080 cell membranes, as evidenced by the intense band at 5 min. More broadly, the data confirm the EGFR-binding capability of EGF-nanoceria. However, it is unexpected that the intensities of the EGFR bands for the control and APTES-nanoceria are different at 5 min when the absence of EGF in both should have generated similar intensities. This difference is attributed to the nanoparticle-mediated receptor modulation, where the nanoparticles alone can modulate the activity of the receptors.^{92,93}

3.5 | Cellular uptake of nanoceria by fibrosarcoma cells

The TEM imaging shown in Figure 6 demonstrates the cellular uptake of nanoparticles by fibrosarcoma cells. The images from the early time points of 1, 2, and 5 min indicate the presence of nanoparticles in the vicinity of the cell membrane and the possible interaction with the cell membrane. The latter is confirmed by the western blotting data of Figure 5, as shown by the high-intensity band after 5 min of treatment

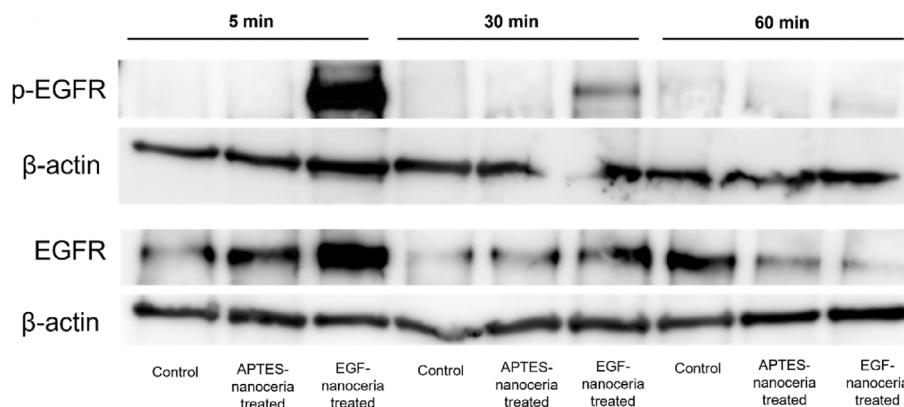


FIGURE 5 Western blot analysis of cell lysates collected after treatment with nanoparticle formulations.

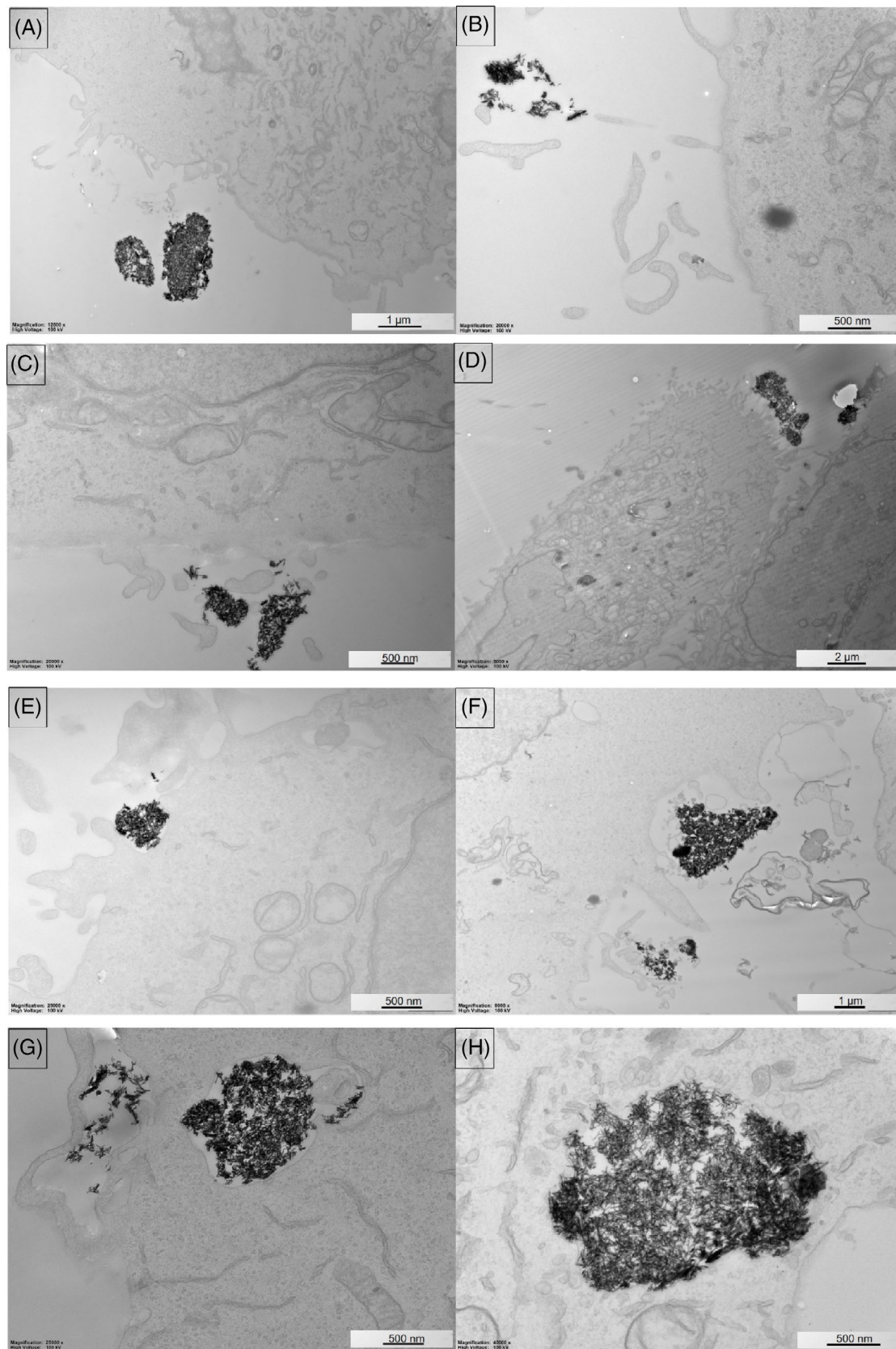


FIGURE 6 TEM imaging of cellular uptake of nanoceria and EGF-nanoceria by HT1080 cells: (A) APTES-nanoceria - 1 min, (B) EGF-nanoceria - 1 min, (C) APTES-nanoceria - 2 min, (D) EGF-nanoceria - 2 min, (E) APTES-nanoceria - 5 min, (F) EGF-nanoceria - 5 min, (G) APTES-nanoceria - 30 min, (H) EGF-nanoceria - 30 min. APTES, amino-propyl-triethoxysilane; EGF, epidermal growth factor.

with the EGF-nanoceria. The images after 30 min of treatment illustrate the cellular uptake of both nonfunctionalized and functionalized nanoceria, where the nanoparticles are enclosed within membrane-bound vesicles, which are likely to be endosomes.^{94,95}

These images also indicate the following points:

1. The nanoceria is highly agglomerated.
2. The APTES-nanoceria agglomerates are smaller than the EGF-nanoceria agglomerates, which is confirmed by the DLS data of Figure S7 (Data S1) and Table 1.
3. The agglomerates increase in size with time, confirming that all of the agglomerates are soft.
4. The agglomerates become more rounded with time, which is as expected.
5. Since the DLS data did not indicate the presence of monodisperse particles, their presence confirms that: (a) the agglomerates are soft and (b) they can be broken up in both the physiological and cell environments. As confirmed by TEM images, no intergrowths are observed between the nanoparticles and therefore the nanoparticles can be considered to be monodisperse. Nevertheless, they possess the tendency to agglomerate quickly in suspension, which explains the absence of monodisperse particles in the DLS data. Hence, the nanoparticles were subjected to ultrasonication immediately prior to their addition to cells, thereby breaking up the agglomerates and allowing their cellular uptake.
6. The rounded porous agglomerates of EGF-nanoceria, which are encapsulated within vesicles, at 30 min are as large as $>2 \mu\text{m}$.
7. The porous nature of the agglomerates does not preclude their catalytic activity because: (a) the individual nanoparticles are in point contact and hence physisorbed only, (b) the soft agglomerates can be broken up into individual nanoparticles, and (c) the high surface areas of the individual nanoparticles remain available once the nanoparticles are released from the vesicles and de-agglomerated.

The confocal microscopy images for FITC-tagged EGF-nanoceria at two magnifications shown in Figure 7 confirm the uptake of EGF-nanoceria, as indicated previously in the data of Figure 4. These images and those of Figure 6 also indicate the following points:

1. 5 min: The nanoparticles are present as large agglomerates on the surfaces of the cells.
2. 30 min: The nanoparticles are partially de-agglomerated and partially internalized.
3. 5 h: The nanoparticles are highly de-agglomerated and partially internalized.

While these data confirm the preceding comments made about agglomeration and de-agglomeration, they also show that cellular uptake occurs within 5 h. Moreover, these data serve as more direct evidence for the demonstration of EGFR-mediated uptake of EGF-nanoceria since the fluorophore was tagged with EGF, thereby confirming the EGFR targeting potential of EGF-nanoceria.

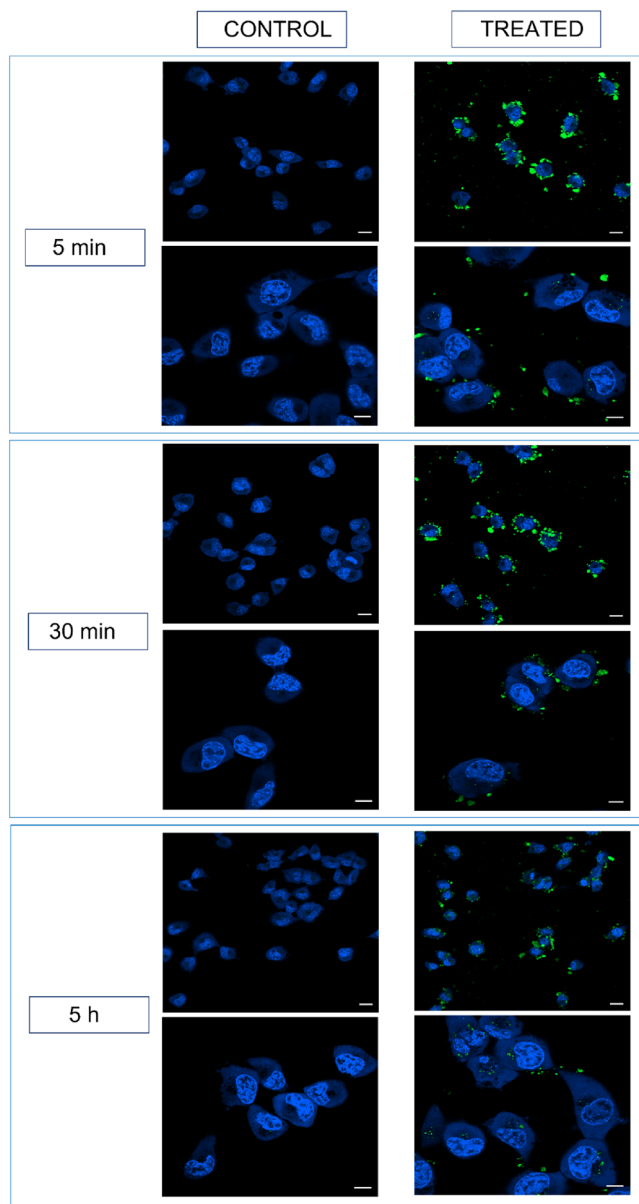


FIGURE 7 Confocal imaging of FITC-tagged EGF-nanoceria (green), showing cellular uptake by HT-1080 cells (blue: Hoechst) (each time point: top row = 20 X, bottom row = 63 X; scale bar: $20 \mu\text{m}$ [20 X] and $10 \mu\text{m}$ [63 X]; 20 X and 63 X images taken at different fields of view (FoV), and hence the densities of nanoparticles in each cell are not directly comparable). EGF, epidermal growth factor; FITC, fluorescein-5-isothiocyanate.

3.6 | Cytotoxicity of nanoceria against tumor cells and normal cells

The metabolic activity of cells is known to decrease the pH,⁹⁶ which can induce ROS generation and adsorption, followed by cell death. However, unlike the previous testing protocols, these samples were subjected to a change in medium every 24 h with the aim of maintaining a physiological pH. Consequently, the ROS generation deriving from the cell metabolism may be a cause of the logarithmic decrease

in the viability of the normal fibroblast cells (MRC-5) shown in Figure 8. This is likely to be a result of an accumulation effect of the nanoceria following the charge-dependant uptake of APTES-nanoceria, which is likely to have manifested through subcellular redistribution of the nanoceria in the organelles. In support of this, aminated positively-charged nanoceria have been found to be internalized by normal cells, thereby inducing subsequent toxicity through lysosomal localization. Since lysosomes are acidic in nature, they would trigger the pro-oxidant nature of nanoceria.⁹⁷ It is remarkable that the nanoceria induced minimal toxicity toward normal cells up to 48 h. Thus, when translating the system to in vivo conditions, the toxicity arising from the time-dependent accumulation effect and possibly the pH effect as well would be likely to be negligible as exocytosis and nanoparticle clearance mechanisms are relatively rapid and occur in less than this time frame.^{98,99}

Concerning the cancer cells the trend is different, where there is a significant decrease in the cell viability all three time points. At the first time point of 24 h, the cell viability decreased to $62 \pm 7\%$ (Figure 8), which is statistically *distinguishable* from the $44 \pm 8\%$ of Figure 2. In principle, these two sets of results should be identical because the cell viability testing with (Figure 8) and without (Figure 2) medium change applies only to the 48 and 72 h time points. Table 1 shows that the $[\text{Ce}^{3+}]$ increased by $\sim 19\%$ from October 2018 to February 2022. As Ce^{4+} is known to be cytotoxic to cancer cells,^{7,100}

the aging of CeO_2 should decrease the cytotoxicity. Since the data in Figure 8 were obtained on May 2021 and those in Figure 2 were obtained on October 2021 earlier, then these results are not consistent with the effect of aging on the $[\text{Ce}^{3+}]$. This disagreement suggests that the role of the active sites in the form of $\text{V}_\text{O}^{\bullet}$,^{75,76} which are generated by $2(\text{Ce}^{4+} \rightarrow \text{Ce}^{3+})$ reductions, for ROS generation from the active sites (producing H_2O_2)⁷ dominate the role of the ROS generation from the $\text{Ce}^{3+} \rightarrow \text{Ce}^{4+}$ oxidation (producing $\bullet\text{OH}$ and $\bullet\text{O}_2^-$). This is consistent with the observation that H_2O_2 is the most long-lived ROS¹⁰¹ and so induces considerable cytotoxicity on cancer cells.^{102,103} However, the effect of the medium is clear in that the cell viability at 48 h decreased to $35 \pm 2\%$. (Figure 8), which is statistically *distinguishable* from the $53 \pm 6\%$ of Figure 2. After 72 h, the cell viability decreased to $45 \pm 4\%$ (Figure 8), which again is statistically *distinguishable* from $89 \pm 1\%$ of Figure 2. Since the statistically significant decrease in cell viability in the HT-1080 cells is analogous to the trend in the MRC-5 cells, then this suggests that the pH did not have a dominant effect with the cancer cells. Thus, it is likely again that an alternative mechanism provides the dominant mechanism for the trend of cell viability. In this case, it is likely to be the reduction in blockage of catalytically active sites owing to the removal of cell debris during change of medium. Thus, the catalyst surfaces remain less impeded from the catalytic generation of ROS and associated cell death.

4 | CONCLUSION

Nanoceria has been fabricated by low-temperature (60°C) hydrothermal synthesis and coated using APTES linker and functionalized with EGF or EGF-FITC. The nanoparticles were examined initially by mineralogical, morphological, structural, particuological, and chemical, characterization. The nanoparticles consisted of rod-shaped nanoceria of dimensions ~ 50 nm length and ~ 12 nm width. The suspension of functionalized nanoceria in water resulted in the formation of multimodal soft agglomerates (≤ 400 nm), where APTES coating yielded positively charged nanoparticles and EGF functionalization yielded negatively charged nanoparticles. The nanoceria surfaces were highly defective, exhibiting $[\text{V}_\text{O}^{\bullet}]$ of $\sim 70\%$ – 80% of the theoretical maximum (25%); aging over 41 months increased the $[\text{V}_\text{O}^{\bullet}]$ from $\sim 17\%$ to $\sim 20\%$ owing to oxygen starvation during storage.

Further examination involved ligand-receptor interaction, cell viability, ROS generation, cellular uptake (quantitative and qualitative), and cytotoxicity toward normal cells. The specificity in the binding of EGF-nanoceria with the EGF receptor (EGFR) was confirmed by western blot analysis. The EGFR-targeting efficiency and the overall anti-cancer performance of EGF-nanoceria were confirmed by comparative examination of APTES-nanoceria and EGF-nanoceria, where the modes of delivery were passive for the former and active for the latter. In comparison with APTES-nanoceria, EGF-nanoceria exhibited enhanced cytotoxicity toward cancer cells, as indicated by the cell viability results, which reflected increased ROS generation levels. However, the percentage cell death decreased over time for both functionalized and nonfunctionalized nanoceria. This is

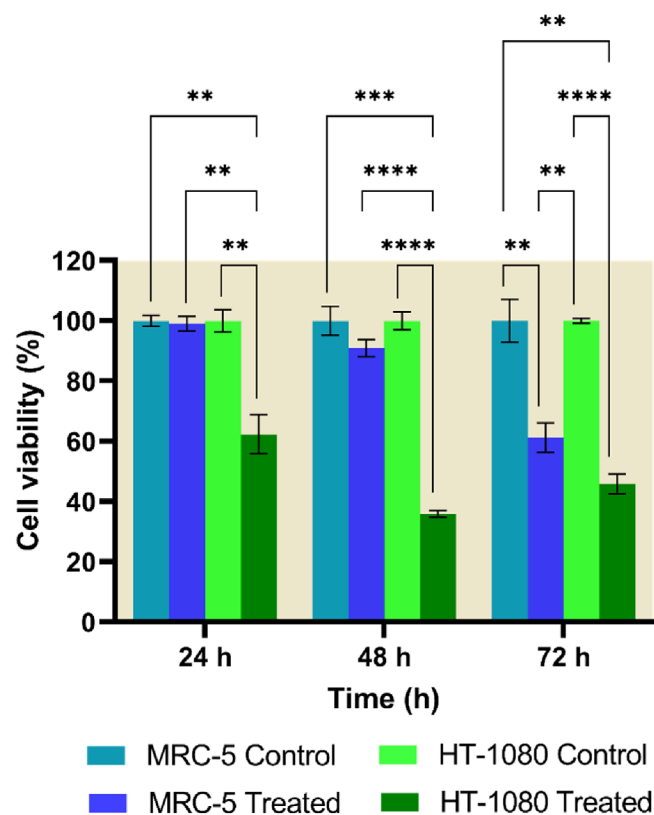


FIGURE 8 Cytotoxicity of APTES-nanoceria toward normal cells (MRC-5) and cancer cells (HT-1080), $**p \leq .01$, $***p \leq .001$, and $****p \leq .0001$. APTES, amino-propyl-triethoxysilane.

attributed to the blockage of active sites on the nanoceria surface by cell debris. However, the ROS generation level for APTES-nanoceria at 72 h was less than that for the control, which is attributed to the elimination of the active site V_O^\bullet by occupation of O ion of the silanol group and/or neutralization of the ROS by charge compensation by the $ROS^+O_2^-$. The cellular uptake revealed a slower rate of uptake by passive delivery for APTES-nanoceria compared to the faster rate of uptake by active delivery for EGF-nanoceria, which maximized at 48 h. The uptake for both types was confirmed by TEM imaging. Further, the FITC-labelling of EGF-nanoceria enabled the imaging of uptake by sarcoma cells using confocal microscopy. The cytotoxicity assay results for APTES-nanoceria revealed that nanoceria exhibited negligible (24 h) and minimal (48 h) toxicity toward normal cells but remarkable cytotoxicity toward cancer cells at all-time points. However, APTES-nanoceria at 72 h induced considerable cytotoxicity toward normal cells owing to a nanoparticle accumulation effect.

Although there is previous work reported the use of nanoceria to target various receptors overexpressed in several cancers, such as the folate receptor^{104,105} and the CD44 receptor,¹⁰⁶ the present work appears to provide the first report of the fabrication and functionalization of nanoceria with EGF with the aim of targeting the EGF receptor. This strategy to target EGFR in cancer has potential widespread applicability as several cancers are reported to be EGFR-positive.^{33,34} The data obtained from the comparative studies for the EGFR-targeted and non-targeted nanoceria reveal significant improvement in the anticancer properties and potential therapeutic performance of EGF-nanoceria through enhanced cellular uptake of nanoparticles, increased generation of ROS, and resultant increased cytotoxicity of nanoceria. Further, FITC-tagged EGF-nanoceria offers considerable potential in the theranostic management of EGFR-positive cancers since the binding of EGF-nanoceria to the receptor and the subsequent detection of fluorescence provide the diagnostic potential in the imaging of such cancers.

AUTHOR CONTRIBUTIONS

Kochurani K. Johnson: Conceptualization; experimental design; nanoparticle synthesis characterization; cell viability, cytotoxicity, ROS generation, cellular uptake level measurement assays; data analysis; writing of initial draft of manuscript. Pramod Koshy: Data analysis support, reviewing and editing of initial and final drafts of manuscript. Michelle Devadason: Western blotting, reviewing of final draft of manuscript. Joanna Biazik: TEM of cellular uptake of nanoparticles and writing of the TEM imaging section of manuscript. Chantal Kopecky: Confocal imaging. Xiaoran Zheng: TEM, XPS and TGA. Yue Jiang: Methylene blue assay, cell viability assay testing the blockage of active sites by cell debris Xiaochun Wang: Assistance with experimental design, preliminary data analysis. Yiling Liu: DLS analysis, writing of DLS analysis section. Jeff Holst: Reviewing and editing of final draft of manuscript. Jia-Lin Yang: Assistance with conceptualization, reviewing of final draft of manuscript. Kristopher A. Kilian: Data analysis support, assistance with experimentation, reviewing and editing of final draft of manuscript. Charles C. Sorrell: Project supervision,

funding acquisition, data analysis, reviewing and editing of all drafts of manuscript.

ACKNOWLEDGMENTS

The authors acknowledge the financial support of the Australian Research Council (Grant No. DP170104130) and the UNSW Sydney Scientia Ph.D. scholarship. K.K.J. acknowledges the technical support offered by Ms. Vina Putra, Ms. Farzaneh Ziaee, and Ms. Yuwen Xu. The authors acknowledge the characterization, cell culture, and imaging facilities provided by the Mark Wainwright Analytical Centre at UNSW Sydney.

DATA AVAILABILITY STATEMENT

The data that support the findings of this study are available from the corresponding author upon reasonable request.

ORCID

Kochurani K. Johnson  <https://orcid.org/0000-0002-4635-714X>

REFERENCES

1. Thakor AS, Gambhir SS. Nano-oncology: the future of cancer diagnosis and therapy. *CA Cancer J Clin*. 2013;63(6):395-418.
2. Arviso RR, Bhattacharyya S, Kudgus RA, Giri K, Bhattacharya R, Mukherjee P. Intrinsic therapeutic applications of noble metal nanoparticles: past, present and future. *Chem Soc Rev*. 2012;41(7):2943-2970.
3. Adeel M, Duzagac F, Canzonieri V, Rizzolio F. Self-therapeutic nanomaterials for cancer therapy: a review. *ACS Appl Nano Mater*. 2020; 3:4962-4971.
4. Nguyen DD, Lai J-Y. Synthesis, bioactive properties, and biomedical applications of intrinsically therapeutic nanoparticles for disease treatment. *Chem Eng J*. 2022;435:134970.
5. Xu Y, Mofarah SS, Mehmood R, Cazorla C, Koshy P, Sorrell CC. Design strategies for ceria nanomaterials: untangling key mechanistic concepts. *Mater Horiz*. 2021;8(1):102-123.
6. Karakoti A, Monteiro-Riviere NA, Aggarwal R, et al. Nanoceria as antioxidant: synthesis and biomedical applications. *JOM*. 2008;60(3): 33-37.
7. Mehmood R, Ariotti N, Yang JL, Koshy P, Sorrell CC. pH-responsive morphology-controlled redox behavior and cellular uptake of nanoceria in fibrosarcoma. *ACS Biomater Sci Eng*. 2018; 4(3):1064-1072.
8. Celardo I, Pedersen JZ, Traversa E, Ghibelli L. Pharmacological potential of cerium oxide nanoparticles. *Nanoscale*. 2011;3(4):1411-1420.
9. Wang Z, Shen X, Gao X, Zhao Y. Simultaneous enzyme mimicking and chemical reduction mechanisms for nanoceria as a bio-antioxidant: a catalytic model bridging computations and experiments for nanozymes. *Nanoscale*. 2019;11(28):13289-13299.
10. Alili L, Sack M, Karakoti AS, et al. Combined cytotoxic and anti-invasive properties of redox-active nanoparticles in tumor-stroma interactions. *Biomaterials*. 2011;32(11):2918-2929.
11. Lord MS, Berret JF, Singh S, Vinu A, Karakoti AS. Redox active cerium oxide nanoparticles: current status and burning issues. *Small*. 2021;17(51):2102342.
12. Pelicano H, Carney D, Huang P. ROS stress in cancer cells and therapeutic implications. *Drug Resist Updat*. 2004;7(2):97-110.
13. Datta A, Mishra S, Manna K, Saha KD, Mukherjee S, Roy S. Pro-oxidant therapeutic activities of cerium oxide nanoparticles in colorectal carcinoma cells. *ACS Omega*. 2020;5(17):9714-9723.

14. Kinnear C, Moore TL, Rodríguez-Lorenzo L, Rothen-Rutishauser B, Petri-Fink A. Form follows function: nanoparticle shape and its implications for nanomedicine. *Chem Rev.* 2017;117(17):11476-11521.
15. Wang W, Gaus K, Tilley RD, Gooding JJ. The impact of nanoparticle shape on cellular internalisation and transport: what do the different analysis methods tell us? *Mater Horiz.* 2019;6(8):1538-1547.
16. Truong NP, Whittaker MR, Mak CW, Davis TP. The importance of nanoparticle shape in cancer drug delivery. *Expert Opin Drug Deliv.* 2015;12(1):129-142.
17. Wei X, Li X, Feng Y, Yang S. Morphology- and pH-dependent peroxidase mimetic activity of nanocerium. *RSC Adv.* 2018;8(21):11764-11770.
18. Johnson KK, Koshy P, Yang JL, Sorrell CC. Preclinical cancer Theranostics—from nanomaterials to clinic: the missing link. *Adv Funct Mater.* 2021;31:2104199.
19. Hoshyar N, Gray S, Han H, Bao G. The effect of nanoparticle size on in vivo pharmacokinetics and cellular interaction. *Nanomedicine.* 2016;11(6):673-692.
20. Dolai J, Mandal K, Jana NR. Nanoparticle size effects in biomedical applications. *ACS Appl Nano Mater.* 2021;4(7):6471-6496.
21. Wang S-H, Lee CW, Chiou A, Wei PK. Size-dependent endocytosis of gold nanoparticles studied by three-dimensional mapping of plasmonic scattering images. *J Nanobiotechnol.* 2010;8(1):1-13.
22. Cruje C, Chithrani B. Integration of peptides for enhanced uptake of PEGylated gold nanoparticles. *J Nanosci Nanotechnol.* 2015;15(3):2125-2131.
23. Lu F, Wu SH, Hung Y, Mou CY. Size effect on cell uptake in well-suspended, uniform mesoporous silica nanoparticles. *Small.* 2009;5(12):1408-1413.
24. Salvioni L, Rizzuto MA, Bertolini JA, Pandolfi L, Colombo M, Prosperi D. Thirty years of cancer nanomedicine: success, frustration, and hope. *Cancer.* 2019;11(12):1855.
25. Blanco E, Shen H, Ferrari M. Principles of nanoparticle design for overcoming biological barriers to drug delivery. *Nat Biotechnol.* 2015;33(9):941-951.
26. Greish K. Enhanced permeability and retention of macromolecular drugs in solid tumors: a royal gate for targeted anticancer nanomedicines. *J Drug Target.* 2007;15(7-8):457-464.
27. Schleich N, Po C, Jacobs D, et al. Comparison of active, passive and magnetic targeting to tumors of multifunctional paclitaxel/SPIO-loaded nanoparticles for tumor imaging and therapy. *J Control Release.* 2014;194:82-91.
28. Pearce AK, O'Reilly RK. Insights into active targeting of nanoparticles in drug delivery: advances in clinical studies and design considerations for cancer nanomedicine. *Bioconjug Chem.* 2019;30(9):2300-2311.
29. Kiparissides C, Kammona O. Nanoscale carriers for targeted delivery of drugs and therapeutic biomolecules. *Can J Chem Eng.* 2013;91(4):638-651.
30. Henry NL, Hayes DF. Cancer biomarkers. *Mol Oncol.* 2012;6(2):140-146.
31. Yu B, Tai HC, Xue W, Lee LJ, Lee RJ. Receptor-targeted nanocarriers for therapeutic delivery to cancer. *Mol Membr Biol.* 2010;27(7):286-298.
32. Sawyers C. Targeted cancer therapy. *Nature.* 2004;432(7015):294-297.
33. Seshacharyulu P, Ponnusamy MP, Haridas D, Jain M, Ganti AK, Batra SK. Targeting the EGFR signaling pathway in cancer therapy. *Expert Opin Ther Targets.* 2012;16(1):15-31.
34. Master AM, Sen Gupta A. EGF receptor-targeted nanocarriers for enhanced cancer treatment. *Nanomedicine.* 2012;7(12):1895-1906.
35. Carpenter G, Cohen S. Epidermal growth factor. *Annu Rev Biochem.* 1979;48(1):193-216.
36. Wee P, Wang Z. Epidermal growth factor receptor cell proliferation signaling pathways. *Cancer.* 2017;9(5):52.
37. Gullick WJ, Marsden JJ, Whittle N, Ward B, Bobrow L, Waterfield MD. Expression of epidermal growth factor receptors on human cervical, ovarian, and vulval carcinomas. *Cancer Res.* 1986;46(1):285-292.
38. Sato O, Wada T, Kawai A, et al. Expression of epidermal growth factor receptor, ERBB2 and KIT in adult soft tissue sarcomas: a clinicopathologic study of 281 cases. *Cancer.* 2005;103(9):1881-1890.
39. Yang JL, Gupta RD, Dawes IW, Crowe PJ. *Potential Application of EGFR Targeted Therapies in Different Types of Sarcomas.* AACR; 2006.
40. Ren W, Korchin B, Zhu QS, et al. Epidermal growth factor receptor blockade in combination with conventional chemotherapy inhibits soft tissue sarcoma cell growth in vitro and in vivo. *Clin Cancer Res.* 2008;14(9):2785-2795.
41. Johnston JB, Navaratnam S, Pitz MW, et al. Targeting the EGFR pathway for cancer therapy. *Curr Med Chem.* 2006;13(29):3483-3492.
42. Troiani T, Martinelli E, Capasso A, et al. Targeting EGFR in pancreatic cancer treatment. *Curr Drug Targets.* 2012;13(6):802-810.
43. Maennling AE, Tur MK, Niebert M, et al. Molecular targeting therapy against EGFR family in breast cancer: progress and future potentials. *Cancer.* 2019;11(12):1826.
44. Okines A, Cunningham D, Chau I. Targeting the human EGFR family in esophagogastric cancer. *Nat Rev Clin Oncol.* 2011;8(8):492-503.
45. Albritton KH, Randall RL. Prospects for targeted therapy of synovial sarcoma. *J Pediatr Hematol Oncol.* 2005;27(4):219-222.
46. Moinfar F, Gogg-Kamerer M, Sommersacher A, et al. Endometrial stromal sarcomas frequently express epidermal growth factor receptor (EGFR, HER-1): potential basis for a new therapeutic approach. *Am J Surg Pathol.* 2005;29(4):485-489.
47. Braun AC, de Mello CAL, Corassa M, et al. EGFR expression in circulating tumor cells from high-grade metastatic soft tissue sarcomas. *Cancer Biol Ther.* 2018;19(6):454-460.
48. Yang J-L, Hannan MT, Russell PJ, Crowe PJ. Expression of HER1/EGFR protein in human soft tissue sarcomas. *Eur J Surg Oncol.* 2006;32(4):466-468.
49. Shevtsov MA, Nicolaev BP, Yakovleva LY, et al. Superparamagnetic iron oxide nanoparticles conjugated with epidermal growth factor (SPION-EGF) for targeting brain tumors. *Int J Nanomedicine.* 2014;9:273-287.
50. Silva CO, Petersen SB, Reis CP, et al. EGF functionalized polymer-coated gold nanoparticles promote EGF photostability and EGFR internalization for photothermal therapy. *PLoS One.* 2016;11(10):e0165419.
51. Tseng CL, Wang TW, Dong GC, et al. Development of gelatin nanoparticles with biotinylated EGF conjugation for lung cancer targeting. *Biomaterials.* 2007;28(27):3996-4005.
52. Mehmood R, Wang X, Koshy P, Yang JL, Sorrell CC. Engineering oxygen vacancies through construction of morphology maps for bio-responsive nanocerium for osteosarcoma therapy. *CrystEngComm.* 2018;20(11):1536-1545.
53. Nicholson RI, Gee JMW, Harper ME. EGFR and cancer prognosis. *Eur J Cancer.* 2001;37:9-15.
54. Pinna A, Malfatti L, Galleri G, et al. Ceria nanoparticles for the treatment of Parkinson-like diseases induced by chronic manganese intoxication. *RSC Adv.* 2015;5(26):20432-20439.
55. Vinzant N, Scholl JL, Wu CM, Kindle T, Koodali R, Forster GL. Iron oxide nanoparticle delivery of peptides to the brain: reversal of anxiety during drug withdrawal. *Front Neurosci.* 2017;11:608.
56. Kochurani KJ, Suganya AA, Nair MG, et al. Live detection and purification of cells based on the expression of a histone chaperone, HIRA, using a binding peptide. *Sci Rep.* 2015;5(1):1-8.
57. Jiang Y, Chen WF, Ma H, et al. Effect of Bi/Ti ratio on (Na_{0.5}Bi_{0.5})TiO₃/Bi₄Ti₃O₁₂ heterojunction formation and photocatalytic performance. *J Environ Chem Eng.* 2021;9(6):106532.

58. Tian X, Zhang L, Jiao Y, Chen J, Shan Y, Yang W. CircABC10 promotes non-small cell lung cancer cell proliferation and migration by regulating the miR-1252/FOXR2 axis. *J Cell Biochem.* 2019;120(3):3765-3772.
59. Chen K, Shi W. Autophagy regulates resistance of non-small cell lung cancer cells to paclitaxel. *Tumor Biol.* 2016;37:10539-10544.
60. Yang Y, Ding L, Li Y, Xuan C. Hsa_circ_0039411 promotes tumorigenesis and progression of papillary thyroid cancer by miR-1179/ABCA9 and miR-1205/MTA1 signaling pathways. *J Cell Physiol.* 2020;235(2):1321-1329.
61. Liu Y, Yang Y, Li L, et al. LncRNA SNHG1 enhances cell proliferation, migration, and invasion in cervical cancer. *Biochem Cell Biol.* 2018;96(1):38-43.
62. Cai L, Qin X, Xu Z, et al. Comparison of cytotoxicity evaluation of anticancer drugs between real-time cell analysis and CCK-8 method. *ACS Omega.* 2019;4(7):12036-12042.
63. Hsiao I-L, Bierkandt FS, Reichardt P, et al. Quantification and visualization of cellular uptake of TiO₂ and Ag nanoparticles: comparison of different ICP-MS techniques. *J Nanobiotechnol.* 2016;14(1):1-13.
64. Tamizhdurai P, Sakthinathan S, Chen SM, Shanthi K, Sivasanker S, Sangeetha P. Environmentally friendly synthesis of CeO₂ nanoparticles for the catalytic oxidation of benzyl alcohol to benzaldehyde and selective detection of nitrite. *Sci Rep.* 2017;7(1):1-13.
65. Schilling C, Hofmann A, Hess C, Ganduglia-Pirovano MV. Raman spectra of polycrystalline CeO₂: a density functional theory study. *J Phys Chem C.* 2017;121(38):20834-20849.
66. Zamiri R, Abbastabar Ahangar H, Kaushal A, et al. Dielectrical properties of CeO₂ nanoparticles at different temperatures. *PLoS One.* 2015;10(4):e0122989.
67. Choi Y, Abernathy H, Chen HT, Lin MC, Liu M. Characterization of O₂-CeO₂ interactions using in situ Raman spectroscopy and first-principle calculations. *ChemPhysChem.* 2006;7(9):1957-1963.
68. Babitha KK, Sreedevi A, Priyanka KP, Sabu B, Varghese T. Structural characterization and optical studies of CeO₂ nanoparticles synthesized by chemical precipitation. *Ind J Pure Appl Phys.* 2015;53(9):596-603.
69. Li J, Chen L, Liu N, Li S, Hao Y, Zhang X. EGF-coated nanodendriplexes for tumor-targeted nucleic acid delivery in vivo. *Drug Deliv.* 2016;23(5):1718-1725.
70. Sorrell CC, Taib H, Palmer TC, Peng F, Xia Z, Wei M. Hydroxyapatite and other biomedical coatings by electrophoretic deposition. *Biological and Biomedical Coatings Handbook: Processing and Characterization.* CRC Press-Taylor & Francis Group; 2011:81-137.
71. Jiménez-García G, Lasa H, Quintana-Solórzano R, Maya-Yescas R. Catalyst activity decay due to pore blockage during catalytic cracking of hydrocarbons. *Fuel.* 2013;110:89-98.
72. Haider MR, Jiang WL, Han JL, et al. In-situ electrode fabrication from polyaniline derived N-doped carbon nanofibers for metal-free electro-Fenton degradation of organic contaminants. *Appl Catal B Environ.* 2019;256:117774.
73. Thomas N, Dionysiou DD, Pillai SC. Heterogeneous Fenton catalysts: a review of recent advances. *J Hazard Mater.* 2021;404:124082.
74. Liu W, Tkatchenko A, Scheffler M. Modeling adsorption and reactions of organic molecules at metal surfaces. *Acc Chem Res.* 2014;47(11):3369-3377.
75. Yu K, Lou LL, Liu S, Zhou W. Asymmetric oxygen vacancies: the intrinsic redox active sites in metal oxide catalysts. *Adv Sci.* 2020;7(2):1901970.
76. Zhang N, Tsang EP, Chen J, Fang Z, Zhao D. Critical role of oxygen vacancies in heterogeneous Fenton oxidation over ceria-based catalysts. *J Colloid Interface Sci.* 2020;558:163-172.
77. Zhang J, Lou X, Jin L, et al. Necrosis, and then stress induced necrosis-like cell death, but not apoptosis, should be the preferred cell death mode for chemotherapy: clearance of a few misconceptions. *Oncoscience.* 2014;1(6):407-422.
78. Ölander M, Handin N, Artursson P. Image-based quantification of cell debris as a measure of apoptosis. *Anal Chem.* 2019;91(9):5548-5552.
79. Piao H, McIntyre NS. Adventitious carbon growth on aluminium and gold-aluminium alloy surfaces. *Surf Interface Anal.* 2002;33(7):591-594.
80. Boedtker E, Pedersen SF. The acidic tumor microenvironment as a driver of cancer. *Annu Rev Physiol.* 2020;82:103-126.
81. Riemann A, Schneider B, Ihling A, et al. Acidic environment leads to ROS-induced MAPK signaling in cancer cells. *PLoS One.* 2011;6(7):e22445.
82. Saavedra-García P, Roman-Trufero M, Al-Sadah HA, et al. Systems level profiling of chemotherapy-induced stress resolution in cancer cells reveals druggable trade-offs. *Proc Natl Acad Sci.* 2021;118(17):1-12.
83. Jana SK, Banerjee P, das S, Seal S, Chaudhury K. Redox-active nanocerium depolarize mitochondrial membrane of human colon cancer cells. *J Nanopart Res.* 2014;16(6):1-9.
84. Damle MA, Shetty VG, Jakhade AP, Kaul-Ghanekar R, Chikate RC. Bi-functional nature of nanocerium: pro-drug and drug-carrier potentiality towards receptor-mediated targeting of doxorubicin. *New J Chem.* 2020;44(39):17013-17026.
85. Seminko VV, Maksimchuk PO, Grygorova GV, Hubenko KO, Yefimova SL. Features of ROS generation during hydrogen peroxide decomposition by nanocerium at different pH values. *Funct Mater.* 2021;28:420.
86. Berktaş I, Ghafar AN, Fontana P, Caputcu A, Menciloglu Y, Okan BS. Facile synthesis of graphene from waste tire/silica hybrid additives and optimization study for the fabrication of thermally enhanced cement grouts. *Molecules.* 2020;25(4):886.
87. Ha HT, Huong NT, Lee BK, et al. Ternary magnetic polymer cross-coupled in [γ-APTES]-dispersion to remove azole compound: economic research and educational policy management. *Res Chem Intermed.* 2020;46(11):5023-5048.
88. Figueroa D, Asaduzzaman M, Young F. Real time monitoring and quantification of reactive oxygen species in breast cancer cell line MCF-7 by 2', 7'-dichlorofluorescein diacetate (DCFDA) assay. *J Pharmacol Toxicol Methods.* 2018;94:26-33.
89. Wang Y, Branicky R, Noë A, Hekimi S. Superoxide dismutases: dual roles in controlling ROS damage and regulating ROS signaling. *J Cell Biol.* 2018;217(6):1915-1928.
90. Vieira AV, Lamaze C, Schmid SL. Control of EGF receptor signaling by clathrin-mediated endocytosis. *Science.* 1996;274(5295):2086-2089.
91. Treda C, Popeda M, Ksiazkiewicz M, et al. EGFR activation leads to cell death independent of PI3K/AKT/mTOR in an AD293 cell line. *PLoS One.* 2016;11(5):e0155230.
92. Mano SS, Kanehira K, Taniguchi A. Comparison of cellular uptake and inflammatory response via toll-like receptor 4 to lipopolysaccharide and titanium dioxide nanoparticles. *Int J Mol Sci.* 2013;14(7):13154-13170.
93. Peuschel H, Sydlik U, Grether-Beck S, et al. Carbon nanoparticles induce ceramide- and lipid raft-dependent signalling in lung epithelial cells: a target for a preventive strategy against environmentally-induced lung inflammation. *Part Fibre Toxicol.* 2012;9(1):1-11.
94. Safi M, Courtois J, Seigneuret M, Conjeaud H, Berret JF. The effects of aggregation and protein corona on the cellular internalization of iron oxide nanoparticles. *Biomaterials.* 2011;32(35):9353-9363.
95. Iversen T-G, Skotland T, Sandvig K. Endocytosis and intracellular transport of nanoparticles: present knowledge and need for future studies. *Nano Today.* 2011;6(2):176-185.

96. Michl J, Park KC, Swietach P. Evidence-based guidelines for controlling pH in mammalian live-cell culture systems. *Commun Biol*. 2019; 2(1):1-12.
97. Asati A, Santra S, Kaittanis C, Perez JM. Surface-charge-dependent cell localization and cytotoxicity of cerium oxide nanoparticles. *ACS Nano*. 2010;4(9):5321-5331.
98. Sakhtianchi R, Minchin RF, Lee KB, Alkilany AM, Serpooshan V, Mahmoudi M. Exocytosis of nanoparticles from cells: role in cellular retention and toxicity. *Adv Colloid Interf Sci*. 2013;201:18-29.
99. Oh N, Park J-H. Endocytosis and exocytosis of nanoparticles in mammalian cells. *Int J Nanomedicine*. 2014;9(Suppl 1):51.
100. Corsi F, Caputo F, Traversa E, Ghibelli L. Not only redox: the multifaceted activity of cerium oxide nanoparticles in cancer prevention and therapy. *Front Oncol*. 2018;8:309.
101. Smolyarova DD, Podgorny OV, Bilan DS, Belousov VV. A guide to genetically encoded tools for the study of H₂O₂. *FEBS J*. 2021;289: 5382-5395.
102. Symons MC, Rusakiewicz S, Rees RC, Ahmad SI. Hydrogen peroxide: a potent cytotoxic agent effective in causing cellular damage and used in the possible treatment for certain tumours. *Med Hypotheses*. 2001;57(1):56-58.
103. Han Y, Chen JZ. Oxidative stress induces mitochondrial DNA damage and cytotoxicity through independent mechanisms in human cancer cells. *Biomed Res Int*. 2013;2013:1-8.
104. Li H, Liu C, Zeng YP, et al. Nanoceria-mediated drug delivery for targeted photodynamic therapy on drug-resistant breast cancer. *ACS Appl Mater Interfaces*. 2016;8(46):31510-31523.
105. Vassie JA, Whitelock JM, Lord MS. Targeted delivery and redox activity of folic acid-functionalized nanoceria in tumor cells. *Mol Pharm*. 2018;15(3):994-1004.
106. Babu Varukattu N, Lin W, Vivek R, et al. Targeted and intrinsic activity of HA-functionalized PEI-nanoceria as a nano reactor in potential triple-negative breast cancer treatment. *ACS Appl Bio Mater*. 2019; 3(1):186-196.

SUPPORTING INFORMATION

Additional supporting information can be found online in the Supporting Information section at the end of this article.

How to cite this article: Johnson KK, Koshy P, Kopecky C, et al. ROS-mediated anticancer effects of EGFR-targeted nanoceria. *J Biomed Mater Res*. 2023;1-16. doi:[10.1002/jbm.a.37656](https://doi.org/10.1002/jbm.a.37656)